Coupled air-sea interaction patterns and surface heat-flux feedback in the Bay of Biscay

G. Esnaola,[1] J. Sáenz,[2] E. Zorita,[3] P. Lazure,[4] U. Ganzedo,[2] A. Fontán,[1] G. Ibarra-Berastegi,[5] and A. Ezcurra[6]

Received 31 October 2011; revised 16 May 2012; accepted 19 May 2012; published 30 June 2012.

[1] The coupled variability of the Sea Surface Temperature (SST) and atmosphere-ocean surface heat fluxes over the Bay of Biscay (Eastern North Atlantic) has been analyzed. Daily surface heat fluxes from different meteorological reanalyses are combined with a high resolution reconstructed satellite SST data set by means of Lagged Maximum Covariance Analysis (MCA). Lagged MCA is applied at different spatial scales. Its results are interpreted within the framework of Hasselmann's stochastic climate model. The surface heat-flux feedback on SST is confirmed to be generally negative. No clear relation is found between the first MCA expansion series and the leading Sea Level Pressure (SLP) patterns. However, a clear relation is found between the second expansion series and the leading SLP Principal Component (PC) when the atmosphere leads the ocean. Spatial patterns of anomalies of the SST and of the SST tendency are found to be related by a 4 day lag. The same reconstructed satellite SST and reanalysis heat fluxes are combined to estimate the feedbacks related to the surface heat fluxes. The traditional procedure used to compute the surface heat-flux feedbacks from monthly data is adapted for daily data. High resolution maps of the heat-flux feedback are derived for the annual and seasonal cases for the Bay of Biscay. Feedbacks related to turbulent (latent and sensible heat) fluxes are shown to dominate over the radiative ones. Special attention is paid to small-scale features present in both Lagged Covariance patterns and surface heat-flux feedback estimates.

Citation: Esnaola, G., J. Sáenz, E. Zorita, P. Lazure, U. Ganzedo, A. Fontán, G. Ibarra-Berastegi, and A. Ezcurra (2012), Coupled air-sea interaction patterns and surface heat-flux feedback in the Bay of Biscay, *J. Geophys. Res.*, *117*, C06030, doi:10.1029/2011JC007692.

1. Introduction

[2] The variability of the surface heat fluxes over the North Atlantic and its relation to atmospheric circulation was analyzed by means of bulk formulae using monthly anomaly fields derived from COADS by *Cayan* [1992a, 1992b] and in simulations with General Circulation Models (GCM) by *Alexander and Scott* [1997]. These studies showed that surface heat-flux anomalies had basin-wide spatial scales, and that sensible and latent heat flux anomalies dominated over the radiative fluxes in midlatitudes. The spatial distribution of the turbulent flux anomalies was related to the atmospheric circulation patterns represented by the leading modes of the Sea Level Pressure (SLP). These studies showed that large scale atmospheric circulation patterns produce characteristic Sea Surface Temperature (SST) anomaly patterns as a result of associated surface fluxes and Ekman transports (see *Deser et al.* [2010] for a review). Instead of using SST anomalies, and based on the heat-budget equation of the mixed-layer [e.g., *Frankignoul*, 1985, equation 9], relations between the SST anomaly tendency and the anomalous heat fluxes were also studied [e.g., *Cayan*, 1992c].

[3] The variation exerted on the surface heat fluxes by existing SST anomalies, previously generated by earlier surface heat fluxes, is known as the surface heat-flux feedback and it is measured as a heat-flux per SST anomaly unit. Given that positive heat-flux anomalies generate positive SST anomalies (fluxes are positive going into the ocean), a negative (positive) feedback will tend to make flux anomalies more negative (positive) and to subsequently dampen (enhance) the SST anomalies. The response of atmospheric General Circulation Models (GCMs) to prescribed SST

[1]Marine Research Division, AZTI-Tecnalia, Pasaia, Spain.
[2]Department of Applied Physics II, Faculty of Science and Technology, University of the Basque Country, Leioa, Spain.
[3]Institute for Coastal Research, Helmholtz-Zentrum Geesthacht, Geesthacht, Germany.
[4]Department DYNECO, IFREMER, Plouzané, France.
[5]Fluid Mechanics and N.I. Department, Engineering School of Bilbao, University of the Basque Country, Bilbao, Spain.
[6]Department of Applied Physics II, Faculty of Pharmacy, University of the Basque Country, Vitoria, Spain.

Corresponding author: G. Esnaola, Marine Research Division, AZTI-Tecnalia, Herrera Kaia Portualdea z/g, E-20110 Pasaia, Gipuzkoa, Spain. (gesnaola@azti.es)

0148-0227/12/2011JC007692

anomalies was the context in which the first estimates of the surface heat-flux feedback were obtained, as reviewed by *Frankignoul et al.* [1998] and *Frankignoul and Kestenare* [2002]. Both positive and negative values for the surface heat-flux feedback were derived, depending on the geographical location and on the spatial scales and seasons analyzed, among other factors. For midlatitude SST anomalies, values of the surface heat-flux feedback were negative and were in general dominated by the turbulent (sensible and latent heat) flux. The interest was later directed toward the analysis of coupled atmosphere-ocean GCMs where the simulated SST anomalies are physically more consistent with the simulated atmospheric circulation, in contrast to simulations driven by prescribed SSTs [*Frankignoul and Kestenare*, 2002].

[4] Estimations of the surface heat-flux feedback for the North Atlantic were also obtained from monthly SST and surface turbulent flux fields derived from COADS observations by *Frankignoul et al.* [1998]. Negative values in the 10–50 Wm^{-2} K^{-1} range were derived. Lower values and a spatially more homogeneous pattern were observed for summer values compared to those for winter. That work was later extended, using monthly data from COADS and from the NCEP reanalysis, by *Frankignoul and Kestenare* [2002] covering a wider area of the Atlantic and the North Pacific. Separated surface heat-flux feedbacks related to the net, and to the turbulent and radiative (short and long wave) fluxes were derived. Negative feedback values within the range of the previous study were derived for the net and turbulent fluxes, both through the whole year and for individual seasons, while weak positive values were obtained for the radiative flux. Turbulent fluxes were dominant and higher values were obtained for winter and autumn, while spring and summer yielded lower values of the feedback. A comparison of the feedback parameter estimations obtained using monthly fields from five coupled models, COADS observations and the NCEP reanalysis was also performed by *Frankignoul et al.* [2004].

[5] Some of these contributions [*Frankignoul and Kestenare*, 2002] aimed to define the shape of the coupled patterns of atmosphere-ocean variability using the technique called MCA (Maximum Covariance Analysis). The patterns explaining the coupled variability of the atmosphere and the ocean in the Atlantic region had already been studied by *Cayan* [1992c], among others, in terms of related patterns of surface heat-flux and SST, and by *Deser and Timlin* [1997] in terms of surface heat-flux and SST tendency.

[6] A review of these results was compiled by *Deser et al.* [2010], where the authors also summarize the main challenges in the analysis of the coupled variability of the atmosphere-ocean system. The first of these challenges is the clarification of the role that high resolution satellite SST measurements could play in the search for coupled variability patterns. The second is to try to understand the role that the surface heat-flux feedback could play in the SST modes observed in mid latitudes that are driven by the atmospheric circulation.

[7] The Bay of Biscay area is located in the eastern Atlantic (Figures 1a and 1b), framed by the west-east oriented Iberian coast and the approximately north-south oriented French coast. The southern part of the bay is characterized by the presence of a narrow continental shelf, while the eastern and northern parts share a wider continental shelf. The net heat fluxes are weak and their values depend on the data set [*Marshall et al.*, 1993; *Large and Yeager*, 2004]. They show a strong variability related to the North Atlantic Oscillation [*Cayan*, 1992c]. Concerning the oceanic circulation, the area is located between the eastern part of subpolar and the subtropical Atlantic gyres, resulting in a general anticyclonic circulation of 1–2 $cm.s^{-1}$ [*Koutsikopoulos and Le Cann*, 1996]. The Iberian Poleward Current (IPC), which carries warm water from the Iberian north-western corner to the inner Bay of Biscay, can also be of special interest for studies related to heat transports [*Garcia-Soto et al.*, 2002].

[8] The first main objective of this paper will be to clarify the role that the use of a high quality and resolution reconstructed SST data set plays in the search for coupled variability patterns, in comparison with previous results obtained using lower resolution data. The second objective consists in an analysis of the sensitivity of the results to the size of the area covered by the coarser heat fluxes when they are combined with a regional high resolution SST data set. Finally, it will also be checked whether small-scale oceanographic features, known to be present in the SST data, give rise to a detectable spatial signal in the coupled variability and surface heat-flux feedback fields.

[9] To meet those goals the paper is organized as follows. Section 2 describes the different data sources and summarizes methodologies used to search coupled patterns. Results are given in section 3. Section 3.1 deals with the search of the coupled patterns of the surface heat fluxes and of both SST anomalies and the SST tendency anomalies. Conversely, section 3.2 deals with the deduction of the surface heat flux feedbacks. A discussion follows in section 4, where the final conclusions are also given.

2. Data and Methodology

2.1. Data

2.1.1. SST Data

[10] Separated day and night satellite SST data for the 1985–2009 period (24 complete years) from the 4 Km resolution AVHRR Pathfinder V5 quality flag 7 product (i.e. best quality pixels only) were obtained and missing values reconstructed using the Data Interpolating Empirical Orthogonal Functions (DINEOF) technique [*Beckers and Rixen*, 2003; *Alvera-Azcárate et al.*, 2005; *Beckers et al.*, 2006; *Alvera-Azcárate et al.*, 2007]. Due to the strict quality requirements applied and restrictions of the technique itself [*Alvera-Azcárate et al.*, 2005; *Beckers et al.*, 2006], data for all days in the period were not available, since only those images with at least 5% of valid data were used. This procedure reduced the number of available days (over 50% of the whole period) but ensured a better quality of the reconstructed SST images. An analysis of the quality of the DINEOF nighttime reconstruction used in this work, is found in Table 1, where the SST reconstructed fields and the original non-missing satellite values are compared with in-situ measurements from the ICOADS data set [*Worley et al.*, 2005]. This table shows that the error of the reconstructed data is basically the same as the error in the original data, but the number of available pixels is much higher.

[11] Figure 1 shows some basic aspects of the daily SST data used. The area covered, shown together with bathymetry

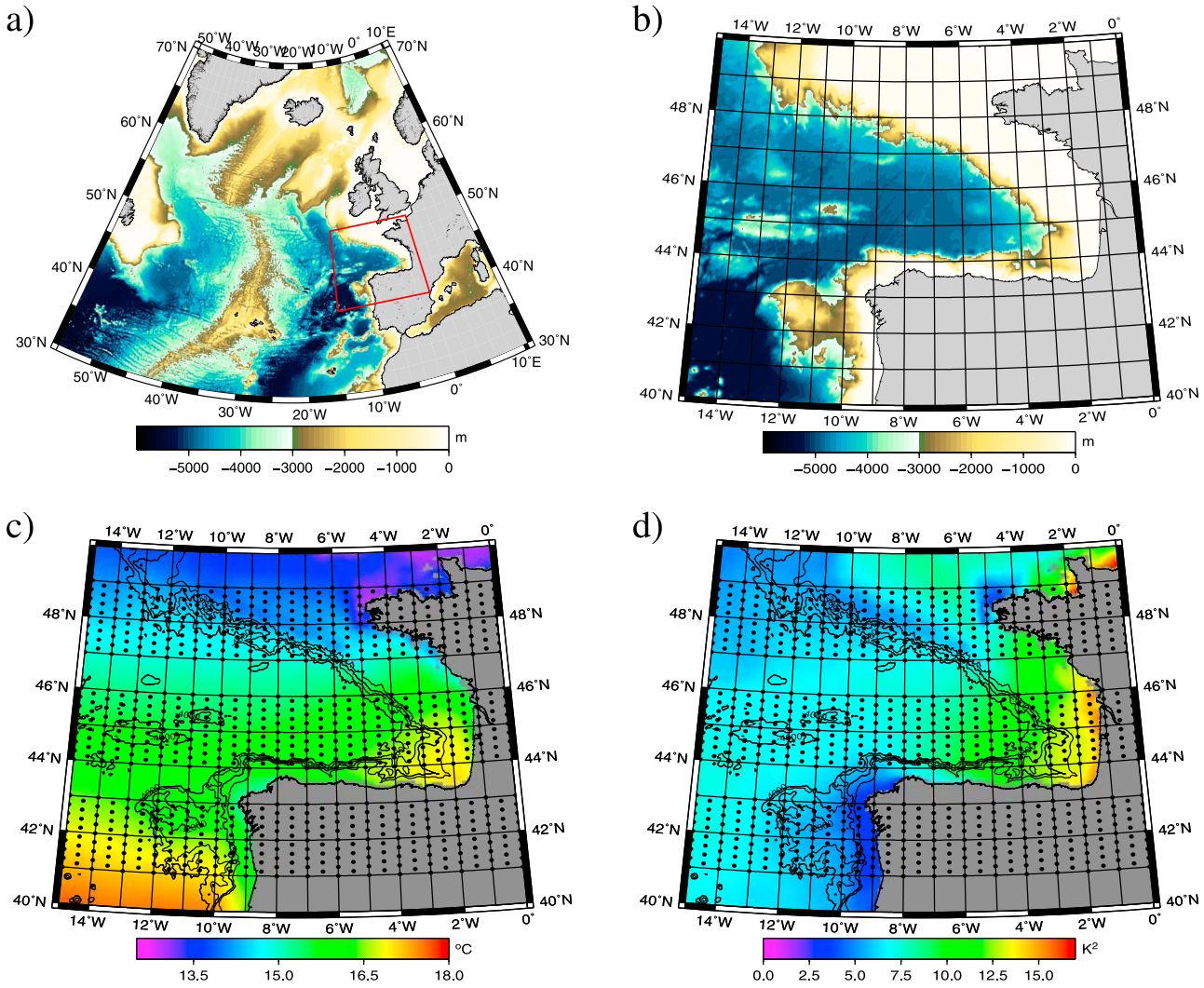

Figure 1. (a) The Bay of Biscay area (red box) and its bathymetry in the context of the North Atlantic, (b) detailed view of the Bay of Biscay, (c) mean sea surface temperature (SST, $^{\circ}C$) over the area and (d) its variance (K^2) obtained from the daily reconstructed SST data set.

within the North Atlantic context in Figure 1a and with more detail in Figure 1b, is slightly larger than the Bay of Biscay. It is relevant to underline that the spatial coverage of the SST data set (15 W–0E, 40 N–50 N) will be fixed to this area for the entire study. Figures 1c and 1d show the average SST and its variance respectively. The mean SST field (Figure 1c) shows a clear north-south gradient, only altered by the presence of an area of higher values in the south-eastern corner of the Bay and lower values in areas around the Brittany coast, as well as in the western coast of the Iberian Peninsula. The variance field (Figure 1d) is substantially influenced by some of the most prominent small-scale oceanographic structures already described in the area, which reinforces the decision to use high-resolution data. Lower variability is observed in the western and north-western coasts of the Iberian Peninsula related to persistent upwelling processes [*Alvarez et al.*, 2008, 2010, and references therein]. Additionally, areas of lower variability can be seen around the Celtic Sea shelf break area related to mixing by internal waves [*Simpson and Hunter*, 1974; *Pingree et al.*, 1986; *New*, 1988; *Pingree and New*, 1995] as well as in the Ushant tidal front [*Mariette and Le Cann*, 1985; *Le Boyer et al.*, 2009] area in the north-western coast of Brittany. The area showing the highest variance covers the entire inner corner of the Bay, with the highest values in the eastern coast of the inner bay related to

Table 1. Verification Results for the Nighttime Original Non-Missing Satellite Data and the Reconstruction Obtained Using In-Situ ICOADS Observations for the 1985–2009 Period[a]

	Satellite Non-Missing	DINEOF SST (*)	DINEOF SST
N	70980	70980	447989
BIAS	−0.117	−0.121	−0.180
R	0.954	0.954	0.940
MAD	0.350	0.353	0.419

[a]Originally non-missing satellite pixels are compared with available in-situ measurements in the first column. The second column shows the same values from the DINEOF reconstruction (*). Finally, all matches between the reconstructed satellite data set and the in-situ data set are shown in the third. The sample sizes of each verification sub sample (N), the bias (BIAS), the Pearson correlation coefficient (R) with the seasonal cycle not removed and the median absolute deviation (MAD) are shown.

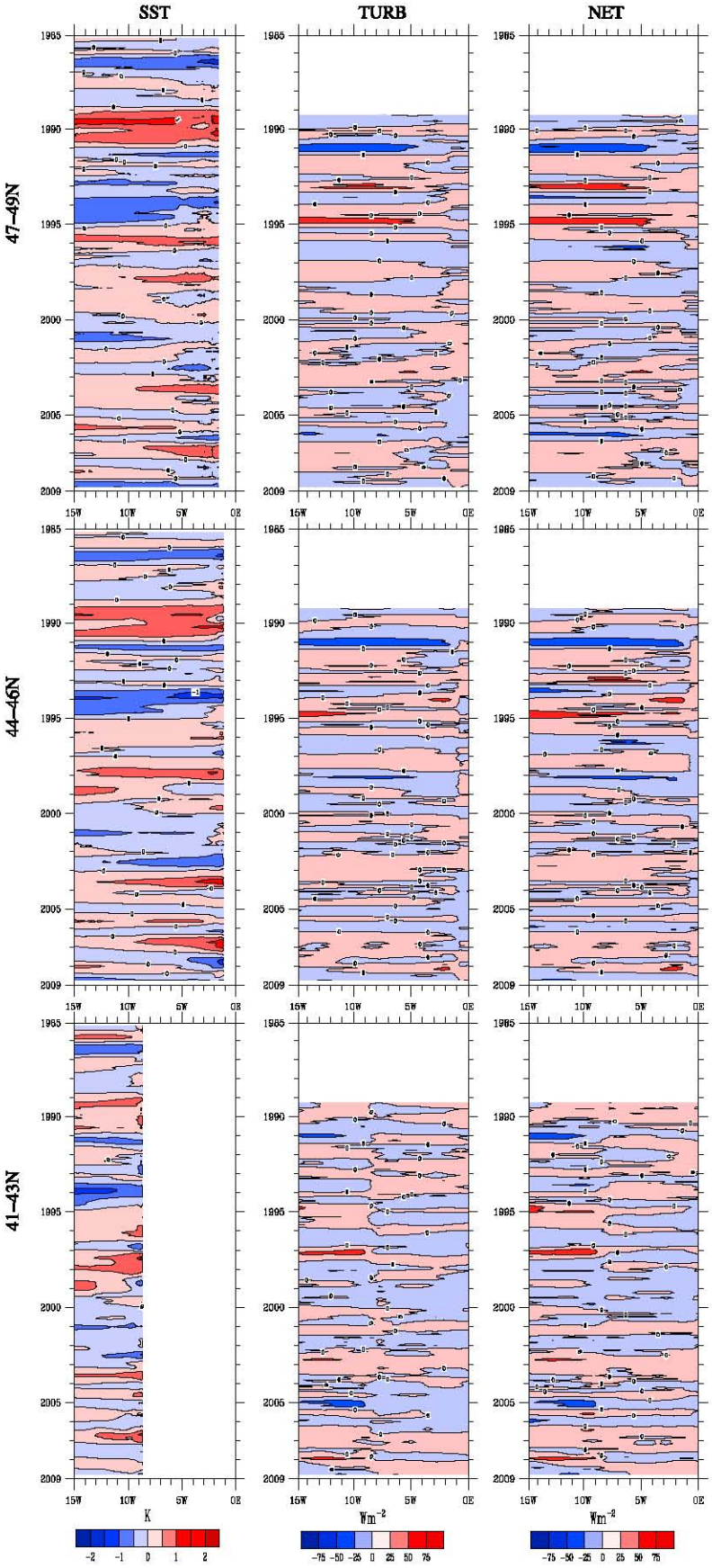
SST
TURB
NET
47–49N
44–46N
41–43N
1985
1990
1995
2000
2005
2009
15W
10W
5W
0E
K
Wm-2
Wm-2

Figure 2

non-persistent upwelling processes and river plumes [*Lazure and Jegou*, 1998; *Puillat et al.*, 2004, 2006; *Lazure et al.*, 2008] amongst other causes. Enhanced values are also observed in coastal areas of the north-eastern part of the domain where tidal effects are important [*Andersen*, 1999].

[12] To provide a view of the time evolution of the SST anomalies over the considered period for the three latitudinal bands marked with dots in Figures 1c and 1d (41 N–43 N, 44 N–46 N and 47 N–49 N), the detrended six-month-moving averaged SST monthly anomalies are shown in the first column of Figure 2. The most remarkable features are observed during the first part of the series (1985–1995) as alternating negative and positive anomalies. These are followed by a period of less marked and less persistent, as well as more local, deviations. Possible causes of that variability are beyond the scope of this work and are thus left for future studies.

2.1.2. Sea Surface Heat-Flux Data

[13] Three sources of surface heat fluxes with different resolution, temporal sampling interval and time coverages have been considered. Surface short wave radiation (SWR), long wave radiation (LWR), sensible heat-flux (SH) and latent heat-flux (LH) were extracted from each of the original data sets. The net flux (NET) and the so-called turbulent flux (TURB) were computed as the sum of all the fluxes and as the sum of the sensible and latent heat fluxes, respectively, for each of the sources. In those cases where the sampling interval of data was 6 hours, night-equivalent fluxes where computed by means of weighted averages [$F(night) = 1/4 * F(18h) + 1/2 * F(00h) + 1/4 * F(06h)$]. Fluxes into the ocean were considered positive by convention.

[14] NCEP/NCAR reanalysis [*Kalnay et al.*, 1996] was the first chosen heat-flux data source. Six hourly data in their approximately $1.9^\circ \times 1.9^\circ$ grid was extracted for the north Atlantic area shown in Figure 1a for the 1985–2009 period.

[15] The second source of surface heat fluxes is the ECMWF ERA-Interim reanalysis [*Simmons et al.*, 2007]. Conceived as a transition product from previous ERA-40 [*Uppala et al.*, 2005] reanalysis product to the forthcoming next generation reanalysis products, ERA-Interim covered only the period 1989–2009 during the realization of this study. Six hourly fluxes in a $0.7^\circ \times 0.7^\circ$ grid for the area shown in the Figure 1a were obtained for the former period. Figure 2 shows the evolution of the de-trended six month moving averaged monthly anomalies of the SST, of the turbulent and net heat fluxes from ERA-Interim, respectively. Visual comparison of these columns clearly indicates that the turbulent fluxes dominate over the radiative ones for these timescales. However, and according to Figure 2, the relationship between the heat-flux and the SST anomalies is not ubiquitous. While some of the heat-flux anomalies seem to have their analogues, or delayed analogues, in the SSTs (e.g. 1991 and 2003), an opposite behavior is observed in other cases (late 1994 and 2005). Thus more research, such as the one conducted in this study, is needed to clarify the overall relationship between these variables.

[16] The third and last source of surface sensible and latent heat flux data is that of the OAFlux project or the OAFluxes [*Yu and Weller*, 2007], which can be found in the Internet site http://oaflux.whoi.edu in combination with ISCCP radiation products [*Zhang et al.*, 2004]. With a $1^\circ \times 1^\circ$ resolution and daily frequency, OAFluxes are built using a combination of reanalysis and satellite products by means of a variational objective analysis procedure (see *Yu and Weller* [2007] for a detailed description). ISCCP radiation products are $1^\circ \times 1^\circ$ daily fields as well.

2.1.3. Sea Level Pressure Data

[17] ERA-Interim 6 hourly Sea Level Pressure (SLP) fields covering the 1989–2009 period were obtained for the North Atlantic (55 W–11E, 29 N–71 N; Figure 1a) and processed to obtain daily nighttime SLP fields. A Principal Component Analysis (PCA) [*von Storch and Zwiers*, 1999; *Wilks*, 2006] was then applied to these fields to obtain the main patterns (EOFs) and expansion series (PCs) characterizing the atmospheric circulation over the North Atlantic during the 1989–2009 period. It is worth noting that the spatial coverage of the SLP fields, unlike the coverage of heat fluxes, remains unchanged throughout the paper.

2.2. Methodology

2.2.1. Maximum Covariance Analysis

[18] Maximum Covariance Analysis (MCA) technique is aimed to find coupled patterns in two data sets [*Bretherton et al.*, 1992; *von Storch and Zwiers*, 1999; *Mo*, 2003; *Wilks*, 2006], namely SST and surface heat fluxes in this case. By means of MCA the anomaly matrices related to two data sets are expanded by a series of mutually orthonormal sets of vectors so that the absolute values of the covariances between their corresponding expansion coefficients are maximized. In practice the expansion vectors (modes) can be obtained by means of a Singular Value Decomposition (SVD) of the covariance matrix C of the two anomaly matrices. Next, they are regressed over original data variables to give them physically interpretable units.

[19] The relative importance of the i-th mode is usually represented by the fraction of the squared covariance it accounts for, given by $\lambda_i/\Sigma\lambda_i$ as a function of the singular values (λ_i) from the SVD analysis. A key aspect of the analysis is that usually a small number of modes accounts for a large fraction of the covariance and, thus, the analysis of the coupled patterns in the data sets can be constrained to a few pairs of modes, provided that the possible degeneracy of the modes is considered [*North et al.*, 1982; *Cheng and Dunkerton*, 1995]. It is worth noting that the polarity of the expansion patterns is not a-priori well defined, since inverse pairs of expansion patterns are equally valid solutions for the MCA problem. This will bear some relevance in the discussion of the results later.

[20] A simple extension of the MCA technique is the so-called Lagged MCA. If the covariance matrix C is computed introducing a time lag between the data sets, then $C(\tau)$ is obtained for a given τ lag (days, months, …) and the application of MCA on $C(\tau)$ is denoted Lagged MCA.

Figure 2. Evolution of the detrended six-month moving averaged monthly anomalies of the (left) sea surface temperature (K), (middle) turbulent (Wm^{-2}) and (right) net (Wm^{-2}) heat fluxes from the ERA-Interim reanalysis for the three latitudinal bands (41 N–43 N, 44 N–46 N and 47 N–49 N) marked with dots in Figures 1c and 1d. For each of the longitudes (horizontal axis) the average of the latitudinal band in the 1985–2009 period is shown (vertical axis.)

[21] Following the two main approaches used in previous studies on the co-variability patterns (see *Deser et al.* [2010] for a review), relationships between the surface heat fluxes and both the SST anomalies and the SST tendency anomalies, will be studied by means of the Lagged MCA technique. The application of the technique proposed here is similar to that used by *Chang et al.* [2001] and *Frankignoul and Kestenare* [2002], and can be understood as a generalization of the procedure. *Chang et al.* [2001] applied MCA to heat-flux and SST anomalies (in addition to wind stress) at 0 lag, whereas *Frankignoul and Kestenare* [2002] repeated the same analysis but for 1 month lag.

[22] For each MCA analysis three results were selected: the total covariance accounted for by all MCA modes (sum of all singular values) and the covariances accounted for by the two leading modes (first and second singular values), as these two together are able to explain most of the covariance.

2.2.2. Surface Heat-Flux Feedback

[23] Coupled variability of the atmosphere-ocean system occurs when one of the subsystems responds to a forcing initially exerted by the other subsystem. For the case of the midlatitude heat-flux anomalies forcing the ocean, the interaction has been described as a two-way interaction with a negative feedback (surface heat-flux feedback), in which the turbulent fluxes dominate [e.g., *Frankignoul et al.*, 1998]. Thus, anomalous heat-fluxes from the atmosphere contribute to the generation of SST anomalies, which in turn modify the heat-fluxes so as to contribute to their dampening.

[24] The theory of stochastic climate models [*Hasselmann*, 1976] offers a framework to determine the sign and magnitude of the surface heat-flux feedback. This concept was first applied to SST anomalies by *Frankignoul and Hasselmann* [1977] showing that statistical properties of midlatitude SST anomalies could be well explained in this context. The theoretical basis was further developed by *Frankignoul* [1985] to take into account all relevant feedbacks. *Von Storch* [2000] further extended the ideas to a group of conceptual models.

[25] Only the basic ideas and assumptions needed to estimate the surface heat-flux feedback from SST and surface heat-flux anomaly data are summarized here. A complete description of the problem, in the formulation used here, can be found in *Frankignoul et al.* [1998] and *Frankignoul et al.* [2004].

[26] Assuming that for a given location the surface heat-flux anomaly H' into the ocean can be decomposed into three terms, a flux term h' independent of the SST anomaly T' in that location, a second term generated by the SST anomaly T' and linearly dependent on it and a third term representing the time persistent linearized influence of the global El Niño-Southern Oscillation (ENSO) teleconnections. Then H' can be written as

$$H'(t) = h'(t) - \lambda T'(t) + \beta N'(t) \quad (1)$$

where the proportionality factor λ ($\mathrm{Wm^{-2}K^{-1}}$) is defined as the surface heat-flux feedback (positive for negative feedback) and β and $N'(t)$ represent the heat flux associated with ENSO and its time behavior respectively. If the persistent signal introduced by ENSO in SST and heat flux anomalies is removed by linear regression to obtain corrected T and H anomalies [*Frankignoul et al.*, 2004], then, for negative τ lags longer than the atmospheric persistence (i.e the *e*-folding time of heat flux anomalies), the feedback parameter can be expressed as

$$\lambda = -R_{TH}(\tau)/R_{TT}(\tau). \quad (2)$$

[27] Here $R_{TH}(\tau)$ is the cross-covariance at lag τ between the corrected SST and heat flux anomalies, i.e. $R_{TH}(\tau) = \langle T(t+\tau)H(t)\rangle$ and $R_{TT}(\tau)$ the lagged auto-covariance of the corrected SST anomalies.

[28] It should be noted that the decomposition (1) and equation (2) assume that the response time of the ocean is fast enough to be neglected. In case that the response time φ can not be neglected [*von Storch*, 2000], the auto-covariance $R_{TT}(\tau)$ must be replaced with $R_{TT}(\tau+\varphi)$ in equation (2), which leads to smaller values of the feedback since $R_{TT}(\tau+\varphi) > R_{TT}(\tau)$ in general. The value of this response time φ will be estimated in this study and the correction applied if necessary.

3. Results

[29] The attention is first pointed, in section 3.1, to the atmospheric forcing on the ocean. Later, in section 3.2, the focus is aimed to the derivation of the feedback exerted on these heat fluxes by the ocean.

3.1. Air-Sea Coupled Patterns

[30] The Lagged MCA method will be first applied to the lagged covariance matrices between SST and surface heat fluxes (net and turbulent fluxes separately). For lags between −30 to 30 days, the analyses were performed at three day lag intervals. For zero to six day lags, however, they were computed for each day lag. In a second step, Lagged MCA was applied to covariance matrices of the tendencies of the SST (*dSST*/*dt* computed by means of centered differences) and surface heat fluxes. The analysis was conducted for the same lag ranges and lag steps as before, but the daily computations are constrained to the range between minus two days to two days lag. A rule of thumb, proposed by *North et al.* [1982] for eigenvalues in EOF analysis and adapted by *Cheng and Dunkerton* [1995] for singular values in SVD, is applied to each of these Lagged MCA computations. To investigate whether heat-flux patterns obtained from the Lagged MCA analysis, which are related to SST or SST tendency, are prominently local or are local manifestations of larger scale patterns, the previous set of computations was also carried out with fluxes covering three different areas going from the local (16 W–2E, 39 N–51 N) to the basin-wide (55 W–11E, 29 N–71 N) scale through an intermediate scale (31 W–5E, 34 N–62 N). The whole Lagged MCA procedure was applied to heat-fluxes from all three ERA-Interim, NCEP and OAFluxes data sets with nearly identical results, so only those related to the ERA-Interim reanalysis will be shown below. Additionally, nearly identical results were obtained for the net and turbulent fluxes for all the calculations made through this section, so only those related to the turbulent fluxes will be analyzed.

[31] Figure 3 shows the results of the Lagged MCA of SST and surface turbulent heat fluxes from the ERA-Interim reanalysis. Each column in the figure is related to one of the geographical domains mentioned before. Figures in the first

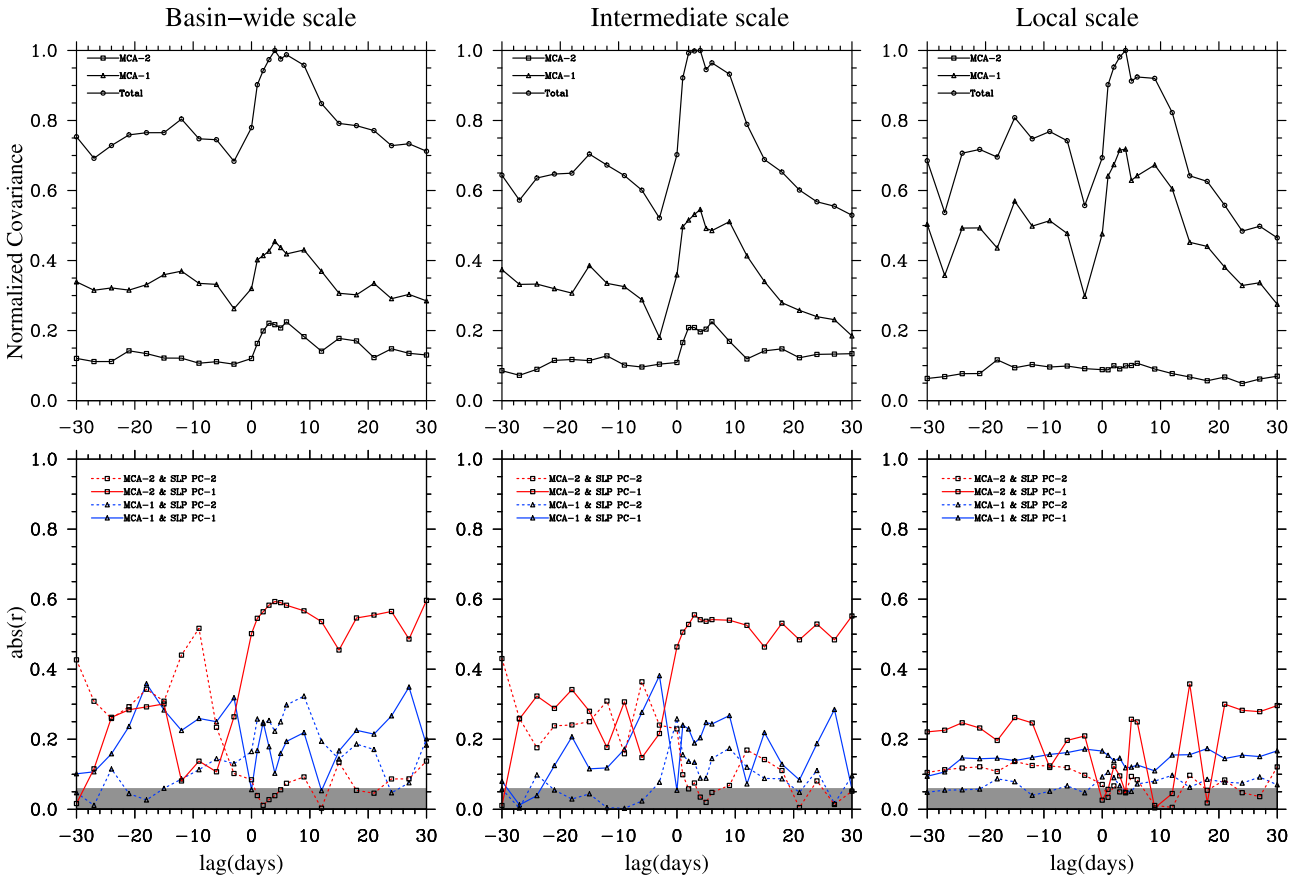

Figure 3. (Top row) Normalized (divided by maximum) covariance curves showing the total covariance (circles) and the covariances related to the first two modes (triangles and squares) as a function of lag obtained from Lagged MCA analyses. First column shows results for the basin-wide scale (55 W–11E, 29 N–71 N), the second for the intermediate scale (31 W–5E, 34–62 N) and the third for the local scale (16 W–2E, 39 N–51 N). (Bottom row) Absolute values of the correlation between the expansion coefficients of the leading two Lagged MCA modes (blue first, red second) and leading two PCs of the North Atlantic (55 W–11E, 29 N–71 N) SLP (solid line for the first PC, dashed for the second PC). Dashed areas indicate values below 95% confidence level under the null-hypothesis of a first order auto-regressive process.

row contain three normalized curves representing, as a function of the time lag, the total covariance accounted for by all modes (circle markers), by the first mode (triangle markers) and by the second one (square markers). The normalization is made by dividing all the curves by the maximum total covariance (sum of all singular values) computed for all analyzed lags. Figures in the second row show, for each of the data sets, the correlations of the synchronous expansion coefficients of the first two MCA modes and the principal components (PCs) of the first two EOFs of the North Atlantic SLP from the ERA-Interim reanalysis (lagged non-synchronous correlations did not show higher values than the synchronous correlations, at least for lags in the ± 1 month range). Note that absolute values of the correlation, and not the correlations themselves, are represented. This is done to avoid the problem of the polarity of the patterns obtained by means of SVD.

[32] According to the stochastic climate model paradigm, in the presence of a negative feedback, negative local covariances are expected for negative lags. Note, however, that in a Lagged MCA that relation will not hold for negative lags for the total covariance or covariances of individual modes, since those are by construction positive. Instead of a change in the sign of the covariance, one would expect a change in the relative polarity of the patterns of one of the variables (SST or flux) from positive to negative. In this case, one could multiply the covariances at negative lags by minus one to obtain the type of curve expected in the context of the stochastic climate model (e.g. Figure 7a). Such change when going from positive to negative lags in the polarity of the spatial patterns can then be used to test the hypothesis of the negative sign of the surface heat-flux feedback [*Frankignoul and Kestenare*, 2002].

[33] Curves in the first row show that the covariance maximum is reached when the atmosphere leads the ocean (positive lag) by around four days. This value is expected to have considerable seasonal modulation. For instance, *Deser and Timlin* [1997] found the lag of maximum covariance to be within the two to three week range for winters in the North Atlantic. Although the analysis of individual seasons is beyond the scope of this work, a preliminary computation for the winter case (JFM) showed the covariance maximum

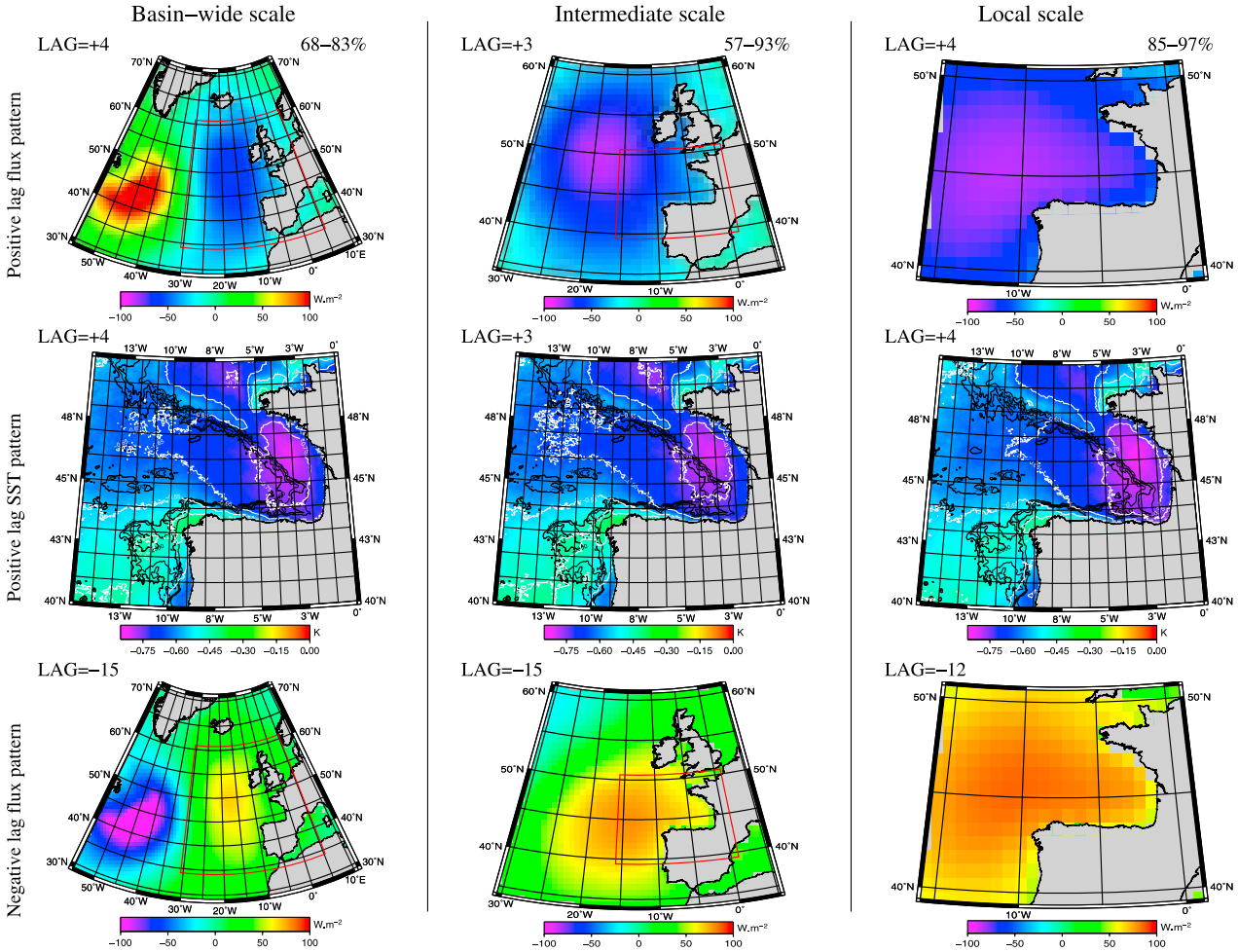

Figure 4. Spatial patterns corresponding to the leading MCA mode of the turbulent heat-flux and the SST anomalies for both (top two rows) positive and (bottom row) negative lags. Three spatial scales are considered for the fluxes while the spatial coverage of the SST patterns is the same for all the analyzed scales. Red boxes in the left and middle columns show the area covered by the image in the right column. Corresponding lags are shown by the figure. Maximum and minimum covariance percentages accounted for by the mode over each scale in the whole range of −30 to +30 day lag are also shown. White lines in the figures of the second row show contour levels from −0.85 to −0.45 *K* using a contour interval of 0.10 *K*.

to occur at a lag of around 18 days, in very good agreement with Deser's and Timlin's result. For the negative lags a secondary maximum is observed at around −15 days, in agreement with the predictions of the stochastic climate model. The relative amplitudes of the maxima for positive and negative lags (larger for positive lag) are consistent with the assumption that the coupled variability is initially generated by the atmosphere [*von Storch*, 2000].

[34] The total covariance shows the same behavior in all three analyzed spatial scales, although the curve tends to become smoother as the scale grows. This result is explained by the fact that the co-variability explained by the MCA mode becomes less local. The same reasoning can be applied to the difference of the total covariance and the covariance of the first mode, which grows with increasing spatial scale. The covariance described by the second MCA mode evolves in parallel with the total covariance for positive lags, with the exception of the local scale that is not able to resolve atmospheric circulation anomaly pattern scales.

[35] Correlations in the second row of Figure 3 indicate to what extent the first two MCA flux modes are linearly related to the two main atmospheric circulation modes derived from PCA analysis of the SLP (explaining 25.4 and 18.6% of the total variance, respectively). Significant correlation for several time lags is observed but there is no clear relationship in general. The exception is the influence, for positive lags, of the leading SLP EOF on the second MCA mode. These correlations show a dependency on whether or not the scale of the fluxes is large enough to resolve the scales of atmospheric circulation. While the basin and mid scales, that fulfill that requirement, show stronger relations, weaker ones are observed for the small scale. This is especially clear for positive lags of the second MCA mode and first SLP PC combination.

[36] Summarizing, Figure 3 shows the existence of a dominant lagged co-variability pattern that is linked to the main atmospheric circulation patterns, but that is not preferentially related to any single SLP pattern. Its covariance resembles the behavior predicted by Hasselman's stochastic climate model for local covariances, with better agreement for small-scale fluxes. Additionally, the MCA shows a second pattern displaying a clear relation with the first EOF of the SLP when the spatial scale of the fluxes can resolve the atmospheric circulation anomaly patterns.

[37] In the following, the spatial patterns obtained for different MCA realizations will be analyzed. To reduce the number of patterns to be shown, those corresponding to the covariance maxima that occurred around $\sim$+4 and ~-15 day lags are selected as representative for positive and negative lag patterns. Additionally, the SST MCA patterns are very similar in the whole range of lags from -30 day to +30 day. Due to this fact, only the SST MCA pattern corresponding to the maximum in the total covariance curve is shown as representative for all lags. Therefore, for each of the spatial scales considered for the heat fluxes a total of three patterns are shown in Figures 4 and 5: two flux patterns corresponding to the mentioned lags and a SST pattern representative for both. The mentioned similarity of the SST patterns for different time lags also allows to easily tackle the previously mentioned polarity problem. Once the representative SST pattern is set, its polarity defines the polarity of the rest of the SST patterns. Subsequently, the polarity of the flux patterns can be adjusted accordingly.

[38] Figures 4 and 5 show, respectively, the first and second modes of the Lagged MCA analysis of the surface turbulent heat-flux and SST anomalies. The three analyzed scales are organized in columns (basin-wide, intermediate and local scales from left to right), corresponding lags are shown and the maximum and minimum percentage of the covariance accounted for by the mode across the range of lags are shown at the top right of each of these columns. Some specific contour levels are shown by white lines in the SST patterns of both figures to enhance the small-scale structures present.

[39] Figure 4 shows a high level of coherence between patterns obtained for the different scales analyzed, both for the fixed scale local SST anomaly patterns and for the scale varying turbulent flux patterns. Both for positive and negative lags, the flux patterns for the smaller scales resemble those of the next larger scale, as in a zooming process. In agreement with the scale considerations mentioned earlier, the best correspondence is observed between basin-wide and mid scales for both positive and negative lags. This correspondence is, however, better for negative lags at small scale and poorer for positive lags of the same scale. It is remarkable that there is a slight reinforcement of the anomaly pattern as the scale decreases, consistent with the mechanisms controlling the scale dependency of the surface heat-flux feedback [*Frankignoul*, 1985; *Frankignoul et al.*, 1998; *Frankignoul and Kestenare*, 2002]. Flux patterns for positive and negative lags have very similar spatial structures but opposite polarity. The negative lag patterns are somewhat shifted south-eastward compared to the positive lag patterns.

[40] The basic spatial structure of the SST anomalies in Figure 4 resembles that of the turbulent heat fluxes. As this occurs for positive lags, it means that the shape of the SST anomaly basically resembles that of the driving fluxes. This resemblance is closer for the smallest scale, which is consistent with the more local character of the MCA results for this scale. Figure 4 supports the hypothesis of a negative surface heat-flux feedback for scales ranging from the basin-wide to the local scale, as the pattern polarity changes when going from the top to bottom of each of the columns in Figure 4. This hypothesis can be summarized by the idea that the surface heat fluxes of a given sign drive the SST (positive lags) to generate anomalies of the same sign, but that they also dampen the generated SSTs (negative lags) as flux anomaly patterns of the opposite sign emerge. Some specific contour levels are drawn in Figure 4 (see figure caption) to highlight the local scale features present in the MCA SST patterns. The decision to use high resolution SST data is now justified as some oceanographic features show their footprint in SST patterns. Detectable are the tongue-like structure over the Celtic Sea shelf break area related to mixing by internal waves [*Simpson and Hunter*, 1974; *Pingree et al.*, 1986; *New*, 1988; *Pingree and New*, 1995], the structure around the Ushant tidal front area [*Mariette and Le Cann*, 1985; *Le Boyer et al.*, 2009] or the strong anomaly area in the inner part of the bay. An additional computation was carried out (not shown) lowering the resolution of the SST data set to that of the reanalysis and repeating the whole procedure. The results showed that the overall structure of the obtained SST patterns remained unchanged, but that a logical loss of small scale details occurred.

[41] Figure 5 shows the patterns related to the second mode for the turbulent fluxes. The patterns related to the basin-wide and mid scales show overall a similar behavior to that of the first mode. As in Figure 4, the mid scale heat flux patterns in Figure 5 match those of the basin-wide scale, a polarity change takes place from negative to positive lags and the SST patterns in the first and second columns of Figure 5 are also very similar. Note that the patterns related to the positive lags of these scales showed the most remarkable relationship with the first PC of the SLP in Figure 3. The patterns of the small scale show discrepancies, however. Although the pattern for negative lag seems to be coherent with those of larger scales, this is not the case for positive lags, as both SST and flux patterns disagree with their large scale counterparts. Consequently, the polarity change criteria is not fulfilled. However, this is not surprising because the small scale was beyond the minimum spatial scale required to resolve the scales of atmospheric circulation anomaly patterns and, consequently, the relationship with the first EOF of the SLP for positive lags was not observed in this scale. Concerning the behavior in SST patterns, a less marked local influence is observed in this case, although the marked anomaly patterns in the northwestern Iberian corner and in the inner Bay French coast may be related to such scale processes.

[42] To take a complementary view of that obtained from the co-variability patterns of the SST and heat-flux anomaly fields, the procedure applied to SST anomaly fields was repeated by using the SST tendency fields instead. An analogous analysis revealed that the time dependent covariance curves peaked for lag zero and then decrease for both positive and negative lags, indicating that ocean response time

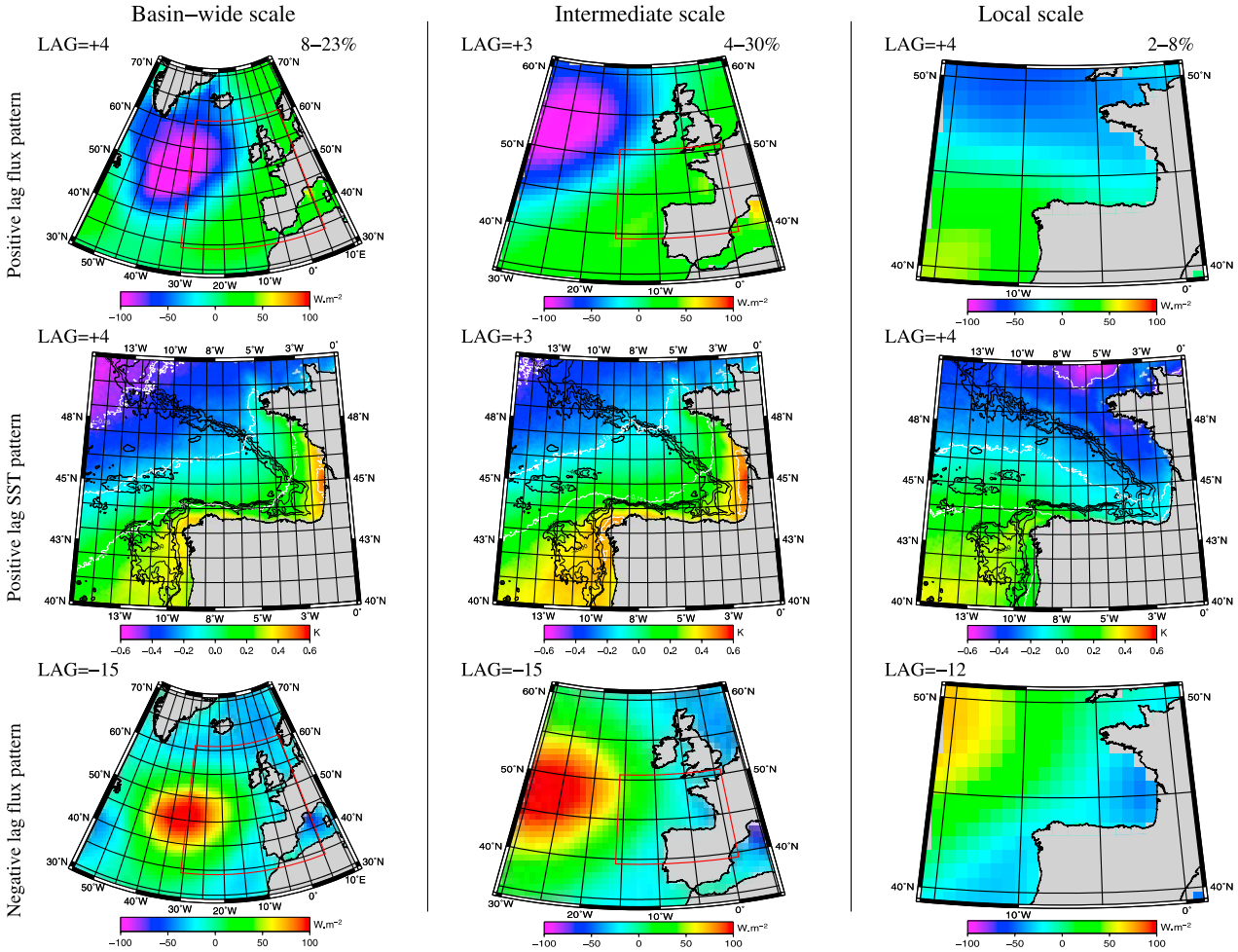

Figure 5. Same as Figure 4 but for the second mode of MCA analysis. White lines in the figures of the second row show contour levels from −0.45 to 0.45 *K* using a contour interval of 0.30 *K*.

can be considered to be close to zero. This means that equation (2) should be used without the ocean response time correction in this area.

[43] Figure 6 shows the patterns obtained from the MCA analysis of the SST tendency and the turbulent fluxes. In this case, the maximum covariance as a function of lag (not shown) has a single peak centered at lag zero. Only the patterns corresponding to this zero lag are shown in Figure 6, which now displays two patterns for each spatial scale considered, instead of the three patterns shown in Figure 4. Once again, heat-flux and temperature patterns obtained for different scales resemble well their larger scale counterparts and the heat-flux patterns are slightly reinforced as the scale decreases. The SST tendency patterns are very similar for the three spatial scales and their shape matches that of the forcing flux patterns. Heat-flux patterns in the first row of Figure 6 are also very similar, although slightly weaker, to the patterns shown in the first row of Figure 4. The similarity between forcing flux patterns in Figures 4 and 6 could indicate that assuming their equivalence as the forcing pattern, the rate of change in SST would be given by patterns in the second row of Figure 6, while the integrated result by those in the same row of Figure 4.

[44] The relation between the SST and SST tendency patterns can also be confirmed by means of the lagged correlations of their corresponding expansion series. In the case that the relationships hold, one would expect correlations to reach a maximum for a lag of about four days for the SST patterns and around lag 0 for the flux patterns, according to the view of a four-day integral of the same forcing flux. In fact, when correlations at different lags between the expansion series of the SST and SST tendency patterns are computed, the largest correlations are obtained for a four-day lag: 0.75 for basin-wide scale, 0.79 for the intermediate one and 0.76 for the local (over the 99% confidence level). The same calculation repeated for the expansion series of the flux patterns yields a maximum one-day lagged correlation of 0.31 (basin-wide), 0.32 (intermediate) and 0.31 (local) (all of them over the 99% confidence level). According to the proposed interpretation, and by comparison with the obtained SST tendency and subsequent SST patterns, it can be concluded that in general the largest anomalies are observed where higher tendency values occur. However, in some areas, such as in the corner of the bay and over the French shelf or the western Iberian coast, the effects are magnified.

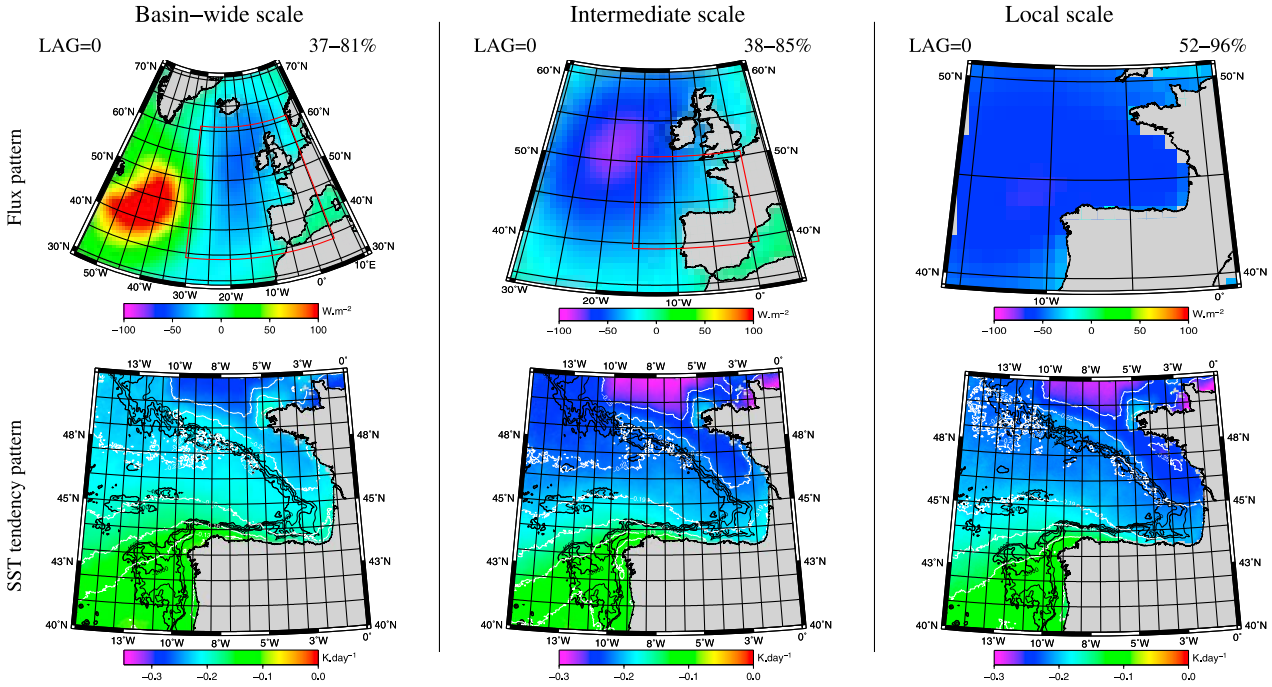

Figure 6. Spatial patterns of the leading MCA mode of the turbulent heat-flux and the tendency of SST over the three spatial scales analyzed. White lines in the figures of the first row show contour levels from -0.25 to -0.10 $K.day^{-1}$ using a contour interval of 0.03 $K.day^{-1}$.

3.2. Surface Heat-Flux Feedback

[45] The ENSO teleconnections can introduce a persistent component in the SST and heat flux anomalies and bias the heat-flux feedback estimated toward positive feedback [*Frankignoul and Kestenare*, 2002; *Frankignoul et al.*, 2004]. As such, that influence has to be removed from both variables, e.g. by means of linear regression analysis.

[46] Among all the available ENSO indices [see, e.g., *Hanley et al.*, 2003], Niño-1+2, Niño-3, Niño-3.4, Niño-4 and MEI were selected (http://www.esrl.noaa.gov/psd/data/climateindices/list) and their relation with SST and heat flux anomalies in the Bay of Biscay area (15 W–0E, 40 N–50 N) was checked by means of a correlation analysis. Significant correlations were found between the net and turbulent fluxes and all indices in the mid and northern parts of the chosen domain for summer (JAS). No significant correlation was found for the radiative ones, with the exception of a small area over the continental shelf south of Brittany for the Niño-3.4 in summer. In the case of the SST field, significant correlations were found for coastal areas off of the western Iberian Peninsula and the southern part of the French continental shelf in autumn (OND) for the Niño-3 and Niño-3.4 indices but the highest correlations were observed for the Niño-1+2 index for the same area and also offshore areas, in autumn and winter (JFM). *Shaman and Tziperman* [2011] proposed a dynamical teleconnection mechanism related to the eastern Pacific ENSO variability, responsible for the positive precipitation anomalies observed, especially in autumn, over the Iberian Peninsula when El Niño conditions are present in the Pacific. The mechanism generates onshore anomalous advection of moisture from the Atlantic ocean to the Iberian Peninsula area and strongest positive precipitation and moisture advection anomalies are located off the western and norther Iberian coasts. These areas are in good agreement with the areas where significant correlations where found for the SST. Since the Niño-1+2 index is related to the eastern corner of the ENSO area and shows the strongest relations with the SST, the ENSO influence was removed from SST and heat flux anomaly data using this index and following the procedure used by *Frankignoul et al.* [2004].

[47] Figure 7 shows the averages for the whole Bay of Biscay area (15 W–0E, 40 N–50 N) of (a) the cross-covariance between the turbulent flux and SST anomalies (R_{HT}), (b) the auto-covariance of the SST anomalies (R_{TT}) and (c) the surface heat-flux feedback (λ), obtained by the combination of R_{HT} and R_{TT} using equation (2) as a function of lag (τ) for the whole year and for also individual seasons (JFM, AMJ, JAS, OND). Auto-covariance of the heat fluxes (R_{HH}) showed an e-folding time of around three days or less. However a longer lag of -15 days was considered to conservatively exclude the influence of the atmospheric persistence (note horizontal axis in Figure 7c). Equation (2) was used without the ocean response time correction to compute the feedback as the atmospheric response can be taken to be close to zero, as discussed in the previous section. The combination of curves in Figure 7a with those in Figure 7b for negative lags longer than the atmospheric persistence yields positive values of the surface heat-flux feedback (recall that λ is positive for negative feedback), as shown in Figure 7c (one value per lag).

[48] Previous works, using monthly data, estimated the heat-flux feedback in each grid point as the average [*Frankignoul and Kestenare*, 2002; *Frankignoul et al.*, 2004], or the weighted average [*Frankignoul et al.*, 1998], of the values obtained for lag -1, -2, -3 months, and for seasonal

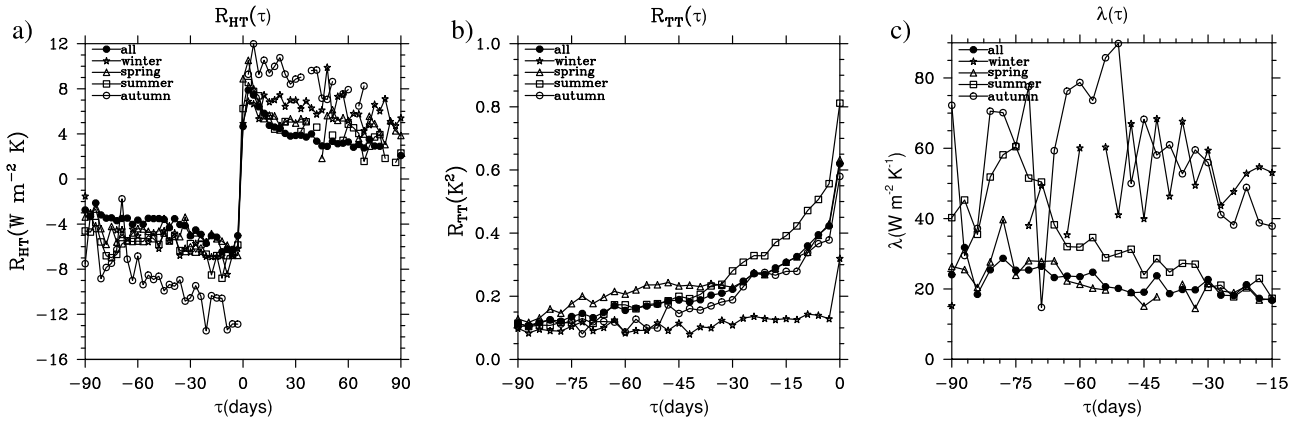

Figure 7. (a) Area average of the cross-covariances between the anomalies of the turbulent heat fluxes from the ERA-Interim reanalysis and the SST anomalies, for the annual and seasonal cases (see labels in figure) as function of the time lag. (b) As in Figure 7a, but for the auto-covariances of the SST anomalies. (c) Feedback values derived for the curves shown in Figures 7a and 7b and from equation (2). Missing values indicate that none of the spatial values of the lag in question were statistical significant.

estimations only those corresponding to lag −1 month. Values in Figure 7c show a tendency to increase with increasing negative lags. Additionally, they also tend to become noisier, especially for seasonal estimations. To avoid those effects only lags equal to or shorter than 30 days will be taken into account. Consequently, the surface heat-flux feedback at every grid point will be estimated by averaging the values obtained for lags in the range of −30 to −15 days, and with a related correlation $r_{HT}(\tau) = R_{HT}(\tau)/[R_{HH}(0)R_{TT}(0)]^{1/2}$ that rejects the null hypothesis that the heat fluxes and the SST are generated by an auto-regressive processes of order 1 (AR1). The threshold of 95% confidence level was estimated by a Monte Carlo test (for each grid point and lag).

[49] Figure 8 shows the spatial maps of feedback parameter λ obtained by applying the previously described procedures to the net (left column), turbulent (mid column) and radiative (right column) fluxes from ERA-Interim reanalysis (first row), NCEP/NCAR reanalysis (second row) and the OAFluxes (third row). Some of the areas do not match the previously stated confidence criteria on r_{HT} and have been masked out (white pixels in the figure). Good agreement can be observed for the net flux among values derived from different data sources, with slightly higher values observed for the OAFluxes. These have their origin in the radiative heat-flux feedback, which is higher in the case of the OAFluxes, especially off the north-western corner of the Iberian Peninsula (as remarked by the white contour lines). The radiative part of the net fluxes in OAFluxes stems from ISCCP radiation products [*Zhang et al.*, 2004], i.e. it is computed independently. The result shown here may thus indicate a disconnection between radiative and turbulent fluxes. Differences in the surface fluxes may also have their origin in the algorithms used in their derivation or in differences in the realization of the surface quantities used to calculate them [*Brunke et al.*, 2011]. However, the results obtained for the three data sources indicate an overall consistent physical behavior.

[50] The sum of turbulent and radiative feedbacks matches very well the feedback for the net flux, with differences in the range of ±1.5 Wm^{-2} K^{-1} for the ERAInterim and OAFluxes and in the range of − 4 − 0 Wm^{-2} K^{-1} for NCEP. Spurious effects due to the land-sea masking can be observed in the two reanalyses, especially across the northern coast of the Iberian Peninsula in the case of NCEP. Identical maps were obtained (not shown) considering lags longer than −30 days and up to −90 days. They showed overall higher values of λ and markedly noisier spatial patterns. This reinforces the methodology applied here and the decision to avoid the use of these lags in the computation of λ as was done in previous works. This is especially important if we take into account that the confidence criteria used here is also more restrictive than the one used in the other studies.

[51] As was pointed out by previous studies, this analysis shows a negative surface heat-flux feedback scenario with the turbulent flux being clearly the largest contributor to the total heat-flux feedback. Values of λ for the net, turbulent and radiative fluxes are in very good agreement with estimations for the Bay of Biscay area obtained in previous works from monthly coarse resolution data [*Frankignoul et al.*, 1998; *Frankignoul and Kestenare*, 2002; *Frankignoul et al.*, 2004]. Concerning the spatial structure of the feedback estimations, an overall spatially homogeneous pattern was found in those previous works using a variety of data for the net and turbulent fluxes, including north-south and west-east gradients or homogeneous patterns. The spatial structure of the feedback maps, in Figure 8, shows lower values in the northern part of the domain for the net and turbulent fluxes. As in the case of the MCA SST patterns, some specific contours (see figure caption) were drawn to enhance the small-scale details of the spatial structure. There seems to be some influence of the bathymetry close to the coast over the French continental shelf from Brittany to the south, where the values are higher than in surrounding areas. Again the use of a high resolution SST data source reveals some degree of modulation by small scale oceanographic processes. Feedbacks in Figure 8 were recomputed (not shown) after lowering the resolution of the SST data set to match the reanalysis. The results showed that the overall observed structure was conserved but the small scale details were lost. Therefore, the use

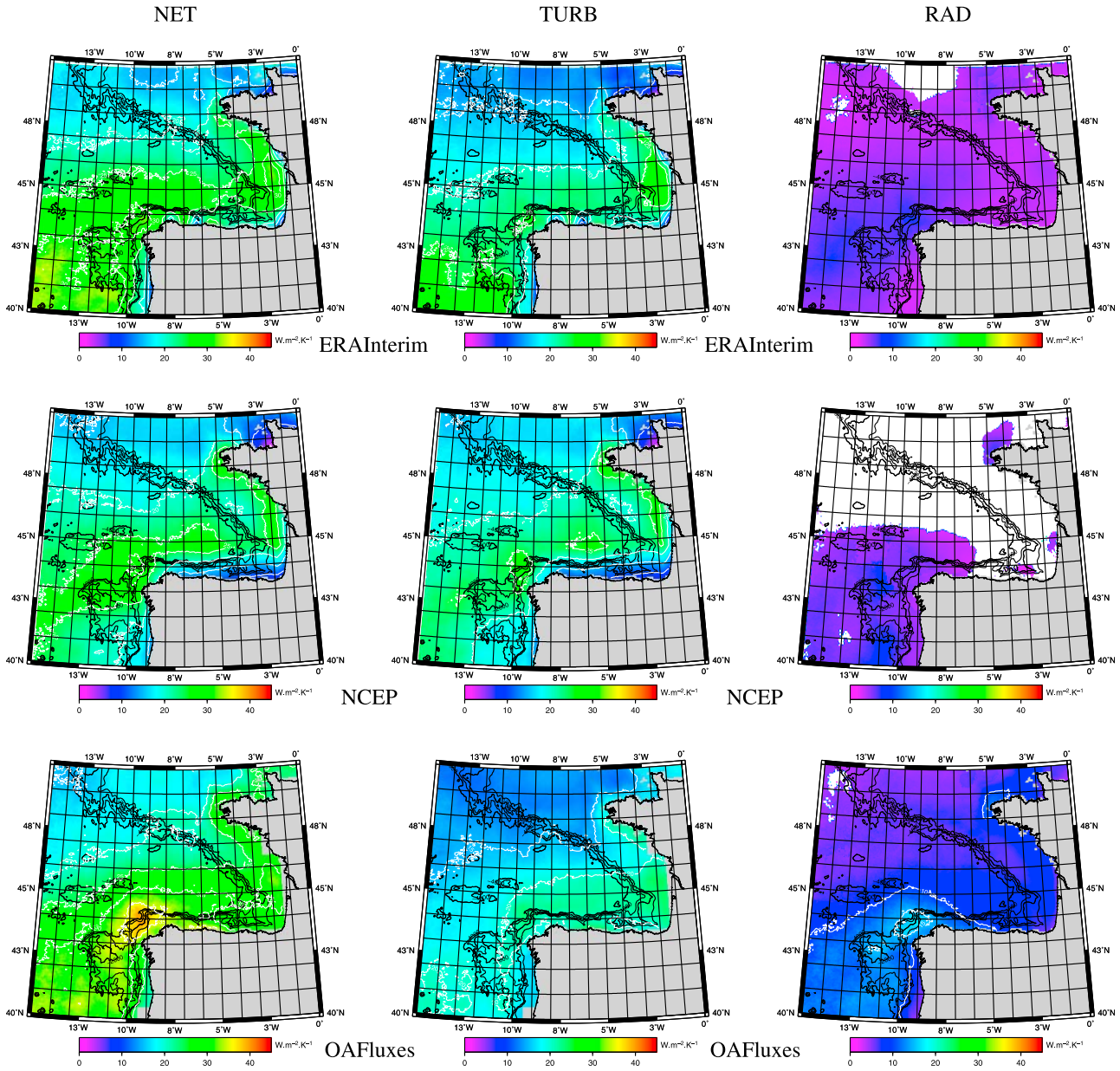

Figure 8. Surface heat-flux feedback maps derived from the (first column) net, (second column) turbulent and (third column) radiative fluxes for each of the three sources of these surface heat fluxes: (first row) ERA-Interim reanalysis, (second row) NCEP reanalysis and (third row) the OAFluxes. White lines show contour levels from 10 to 35 $Wm^{-2}.K^{-1}$ using a contour interval of 5 $Wm^{-2}.K^{-1}$.

of high resolution SST permits to get better spatial information despite the lower resolution of the heat-flux data.

[52] Seasonal scale feedback maps were also computed to analyze the intra-annual variability of the surface heat-flux feedbacks, disaggregated into net and turbulent fluxes. Figure 9 shows the surface heat-flux feedback maps obtained for the turbulent fluxes from ERA-Interim reanalysis (left column), NCEP reanalysis (middle column) and OAFluxes (right column) for individual seasons: winter (JFM, first row), spring (AMJ, second row), summer (JAS, third row) and autumn (OND, fourth row). The maps for the net flux feedback showed a similar relationship (not shown). Some of the areas did not fulfill the statistical confidence criteria and have been masked out, and some specific contour levels were also drawn to enhance the small-scale details of the spatial structure.

Figure 9. Seasonal surface heat-flux feedback maps derived from the turbulent fluxes for each of the three sources of the surface heat fluxes: (first column) ERA-Interim reanalysis, (second column) NCEP reanalysis and (third column) the OAFluxes. (top to bottom) Winter (JFM), spring (AMJ), summer (JAS) and autumn (OND). White lines show contour levels from 20 to 80 $Wm^{-2}.K^{-1}$ using a contour interval of 15 $Wm^{-2}.K^{-1}$.

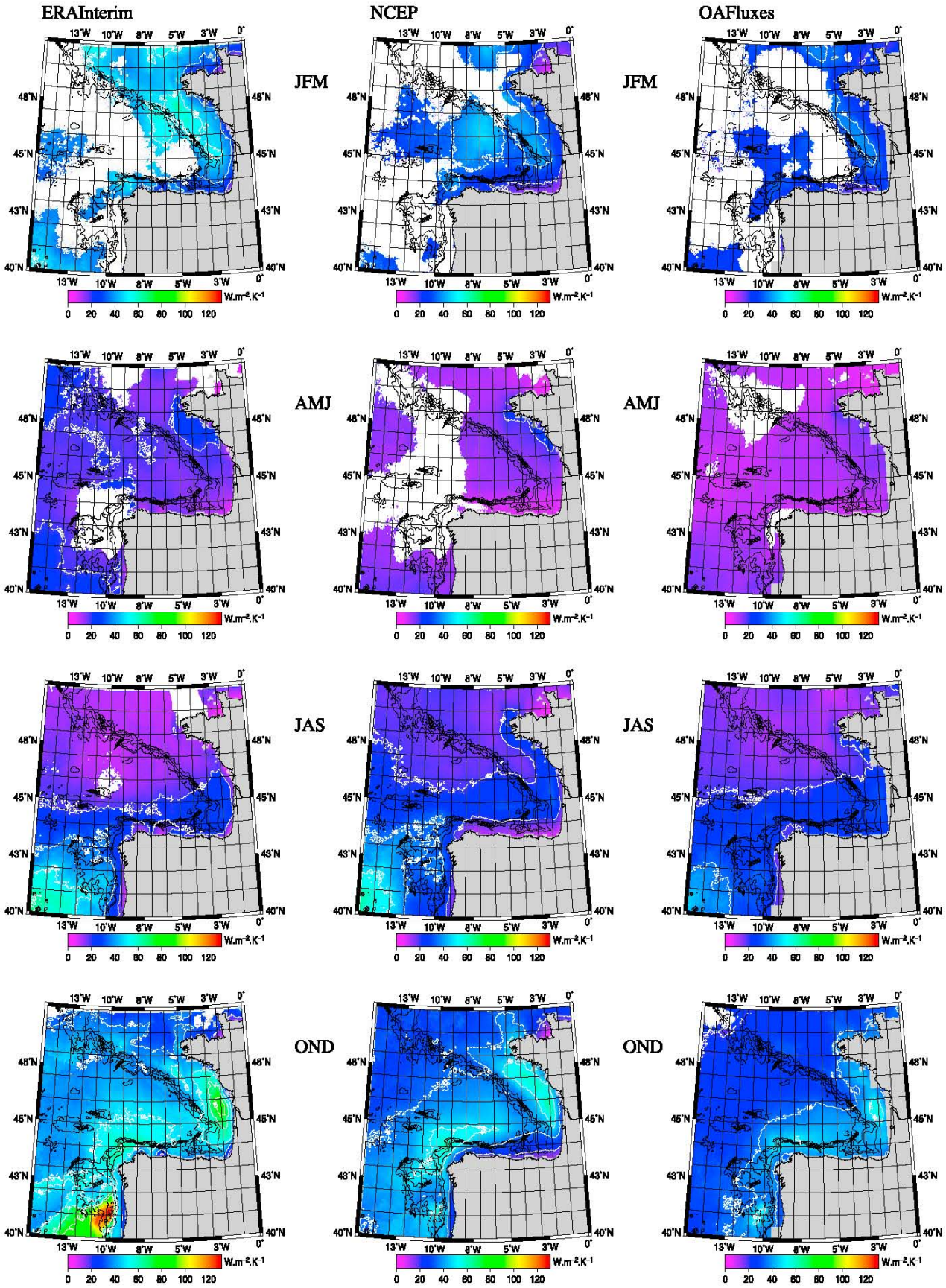
ERAInterim
NCEP
OAFluxes
JFM
AMJ
JAS
OND
13°W 10°W 8°W 5°W 3°W 0°
48°N 45°N 43°N 40°N
W.m⁻².K⁻¹
0 20 40 60 80 100 120

Figure 9

[53] A clear seasonal modulation of the feedback can be observed for all the data sets. The largest values of the feedback occur in autumn and winter and the smallest values in spring and summer, consistent with Figure 7c. As both components of the turbulent flux are directly proportional to the wind speed according to the bulk formulas [i.e., *Frankignoul*, 1985], this seasonal modulation has been attributed to the effect of wind by other authors [*Frankignoul et al.*, 2004]. To separate the effect of the wind from other factors (ocean surface moisture and temperature factors) in the modulation of the feedback, *Park et al.* [2005] used an averaging procedure similar to a Reynold's averaging, which has been applied here as well. The results (not shown) showed that none of the values surpassed the statistical confidence threshold applied in this study. The contribution related to ocean surface moisture and temperature factors showed spatial patterns that were very similar to those shown in Figures 8 and 9, but with larger magnitude.

[54] Different spatial patterns are observed in the individual seasons. An homogeneous pattern with no marked structures is characteristic of the spring feedback, this pattern being very consistent among all three data sources. A coherent spatial pattern among the three sources is also found in summer, when a weak south to north gradient is observed, together with an area of enhanced feedback in the south-western corner. Winter and autumn, on the contrary, yield a spatial pattern which is very sensitive to the data source. In both cases, higher values are observed for NCEP and ERA-Interim reanalyses, especially for the latter. Concerning the small-scale features present in the maps for the autumn case, an area of enhanced values is observed over the French continental shelf. This is the most remarkable pattern, although the structure described close to the French coast in the annual case is also present in some cases.

4. Discussion and Conclusions

[55] Several lines of evidence have indicated a negative surface heat-flux feedback in this study: the inferred properties of the covariance curves in section 3.1, the direct computations in section 3.2 and the polarity change of MCA patterns when going from positive to negative lags. In contrast with previous works that were developed using coarser resolution and monthly frequency data, these results were obtained using daily frequency data and a high resolution SST data set.

[56] Results in section 3.1 from lagged MCA analysis among the heat fluxes and the Bay of Biscay's SST show that covariances behave following Hasselman's stochastic model for local covariances, even though they represent non-local rather than local covariances. It is that way in the cases where the area covered by the heat fluxes is large enough to resolve atmospheric circulation. This implies that when the spatial coverage of the heat flux anomalies is large enough to resolve the main atmospheric circulation patterns (mid scale in this case) the spatial dimension of the SST data set (15 W–0E, 40 N–50 N) is small enough to be considered "local". Additionally, when the spatial coverage of the heat fluxes is large enough, the second MCA mode shows a clear relationship with the first PC of the North Atlantic SLP when the atmosphere is driving the ocean (positive lags). This result stresses the need of a minimum scale to be considered for the atmospheric variables. The first MCA mode, on the contrary, did not show any preferred atmospheric mode driving the variability for the MCA coupled mode, whichever the scale of the fluxes was.

[57] The Lagged MCA conducted for the SST tendency showed that the maximum of the covariance was found to occur for zero lag, indicating that the ocean response can be considered instantaneous and that no correction to the formula to compute the surface heat feedback is required in this area [*von Storch*, 2000]. The forcing flux patterns obtained in that analysis are very similar to the representative forcing flux patterns obtained for $\sim$+4 lag in the case of the SST. Their corresponding expansion coefficients were also shown to be correlated. Therefore, it seems reasonable to interpret the SST patterns as the integral response of the SST tendency patterns. The comparison of these patterns, i.e. second rows of Figures 4 and 6 yields some information on the influence of small scale oceanographic structures in the spatial structure of the patterns. For instance, all the area to the west of the Iberian Peninsula is characterized by lower values in both SST and SST tendency patterns and the structures in both types of patterns are coherent, with the exception of the south-western coast of Iberia where upwelling processes take place [*Alvarez et al.*, 2008, 2010]. Other remarkable differences between the SST tendency patterns and their integral responses occur over the Celtic Sea shelf break related to mixing by internal waves [*Simpson and Hunter*, 1974; *Pingree et al.*, 1986; *New*, 1988; *Pingree and New*, 1995], or to some extent in the Ushant tidal front area [*Mariette and Le Cann*, 1985; *Le Boyer et al.*, 2009]. Also a clear differentiated response is observed in the inner part of the Bay, where strongest values in the SST patterns are observed, probably related to the processes controlling the extra-heating that takes place over that area in spring and summer and that can be detected in Figures 1c and 1d. The eastern French coast in the same inner Bay area shows a differentiated response that may be related to non-persistent upwelling processes and river plumes [*Lazure and Jegou*, 1998; *Puillat et al.*, 2004, 2006; *Lazure et al.*, 2008]. Although further research is needed to elucidate the physical reasons behind such small-scale features, it is clear that the use of a high resolution SST data set confirms the influence of small-scale oceanographic features in the coupled ocean-atmosphere variability.

[58] In this manuscript we compute the surface heat-flux feedbacks out of daily frequency data, while previous estimations [*Frankignoul et al.*, 1998; *Frankignoul and Kestenare*, 2002; *Frankignoul et al.*, 2004; *Park et al.*, 2005] were based on monthly data. Motivated by the convenience of increasing the sample size from which the feedback estimates where computed, some of these previous estimations were averages, or weighted averages, of values obtained for lags of -1, -2, and -3 month, and using only -1 month lag in other cases. However, monthly mean data cannot really resolve the effect of atmospheric persistence. In our case, the effect of atmospheric persistence was bypassed by disregarding negative lags between -15 and 0 days. It was also observed (Figure 7) that the values of the feedback for individual lags tended to become noisy as the lag increased, especially for the winter and autumn. To avoid

this problem, negative lag values longer that −30 days were not used in the computation of the feedbacks. Consequently, the −30 to −15 days lag interval chosen here is consistent with the feedback estimation theory and allows a more precise estimation of feedbacks as the ensemble average over a higher number of realizations. Finally, as the daily data sets are considerably larger than their monthly counterparts, it was possible to define strict confidence intervals for the feedbacks by imposing the requirement that correlation $r_{HT}(\tau) = R_{HT}(\tau)/[R_{HH}(0)R_{TT}(0)]^{1/2}$ should lay over the 95% confidence threshold of the null-hypothesis that the heat fluxes and the SST are an AR1 noise.

[59] Surface heat-flux feedback maps for the annual (Figure 8) and seasonal cases (Figure 9) estimated from three data sources are in good agreement, thus reflecting the dominance of the turbulent fluxes over the radiative ones and a seasonal modulation coherent with previous works [*Frankignoul et al.*, 1998; *Frankignoul and Kestenare*, 2002]. Greater influence of these radiative fluxes is observed in OAFluxes, which could reflect a disconnection of the turbulent and radiative fluxes or also be related to the algorithms used to retrieve the fluxes [*Brunke et al.*, 2011] in the OAFluxes. Concerning the spatial structure of the heat-flux feedbacks, the previous studies showed a variety of results for the Bay of Biscay area. In *Frankignoul and Kestenare* [2002] a low spatial variability was observed for the radiative feedbacks for NCEP reanalysis and COADS database, and also for five global coupled climate models in *Frankignoul et al.* [2004], consistent with the results obtained here. On the contrary, data source dependent higher spatial variabilities were observed in the same studies for the turbulent fluxes. The spatial structure of the turbulent feedbacks obtained here shows a south-north gradient for the annual case, low spatial variability in spring and summer (with the exception of the south-western corner) and higher variability in autumn, all coherent with results in *Frankignoul and Kestenare* [2002]. The effect of small-scale features is not as clear as in the coupled variability analysis by means of Lagged MCA but some influence is detectable, especially over inner French continental shelf in the annual and autumn cases. Future studies will be devoted to the identification of the exact mechanisms conditioning the spatial structure and the mentioned local modulations of the surface heat-flux feedbacks and coupled variability modes computed out of high resolution data sets.

[60] **Acknowledgments.** ERA-Interim data was obtained from the ECMWF data server (http://data.ecmwf.int/data). NCEP Reanalysis data provided by the NOAA/OAR/ESRL PSD, Boulder, Colorado, USA (http://www.esrl.noaa.gov/psd). G. Esnaola is supported by a PhD research grant (Interacción Atmósfera-Océano en el Golfo de Bizkaia) from Fundación Centros Tecnológicos Iñaki Goenaga. The authors acknowledge financial support from projects CGL2008-03321 (Ministry of Science and Innovation, Spanish Government), CTP10-03 PYNATEO and IE10-283 ITSASEUS-II (Basque Government). The authors are thankful for support from UPV/EHU by means of project UFI11/55 and GIU11/01. This is contribution 581 of the Marine Research Division of AZTI-Tecnalia.

References

Alexander, M. A., and J. D. Scott (1997), Surface flux variability over the North Pacific and North Atlantic Oceans, *J. Clim.*, *10*(11), 2963–2978, doi:10.1175/1520-0442(1997)010<2963:SFVOTN>2.0.CO;2.

Alvarez, I., M. Gomez-Gesteira, M. deCastro, and J. M. Dias (2008), Spatiotemporal evolution of upwelling regime along the western coast of the Iberian Peninsula, *J. Geophys. Res.*, *113*, C07020, doi:10.1029/2008JC004744.

Alvarez, I., M. Gomez-Gesteira, M. DeCastro, J. L. Gomez-Gesteira, and J. M. Dias (2010), Summer upwelling frequency along the western Cantabrian coast from 1967 to 2007, *J. Mar. Syst.*, *79*(1–2), 218–226, doi:10.1016/j.jmarsys.2009.09.004.

Alvera-Azcárate, A., A. Barth, M. Rixen, and J. M. Beckers (2005), Reconstruction of incomplete oceanographic data sets using empirical orthogonal functions: Application to the Adriatic Sea surface temperature, *Ocean Modell.*, *9*(4), 325–346, doi:10.1016/j.ocemod.2004.08.001.

Alvera-Azcárate, A., A. Barth, J. M. Beckers, and R. H. Weisberg (2007), Multivariate reconstruction of missing data in sea surface temperature, chlorophyll, and wind satellite fields, *J. Geophys. Res.*, *112*, C03008, doi:10.1029/2006JC003660.

Andersen, O. B. (1999), Shallow water tides in the northwest European shelf region from TOPEX/POSEIDON altimetry, *J. Geophys. Res.*, *104*(C4), 7729–7741, doi:10.1029/1998JC900112.

Beckers, J. M., and M. Rixen (2003), EOF calculations and data filling from incomplete oceanographic datasets, *J. Atmos. Oceanic Technol.*, *20*(12), 1839–1856, doi:10.1175/1520-0426(2003)020<1839:ECADFF>2.0.CO;2.

Beckers, J. M., A. Barth, and A. Alvera-Azcárate (2006), DINEOF reconstruction of clouded images including error maps. Application to the Sea-Surface Temperature around Corsican Island, *Ocean Sci. Disc.*, *3*(4), 735–776, doi:10.5194/osd-3-735-2006.

Bretherton, C. S., C. Smith, and J. M. Wallace (1992), An Intercomparison of Methods for Finding Coupled Patterns in Climate Data, *J. Clim.*, *5*(6), 541–560, doi:10.1175/1520-0442(1992)005<0541:AIOMFF>2.0.CO;2.

Brunke, M. A., Z. Wang, X. Zeng, M. Bosilovich, and C.-L. Shie (2011), An assessment of the uncertainties in ocean surface turbulent fluxes in 11 reanalysis, satellite-derived, and combined global datasets, *J. Clim.*, *24*(21), 5469–5493, doi:10.1175/2011JCLI4223.1.

Cayan, D. R. (1992a), Variability of latent and sensible heat fluxes estimated using bulk formulas, *Atmos. Ocean*, *30*(1), 1–42, doi:10.1080/07055900.1992.9649429.

Cayan, D. R. (1992b), Latent and sensible heat flux anomalies over the northern oceans: The connection to monthly atmospheric circulation, *J. Clim.*, *5*(4), 354–369, doi:10.1175/1520-0442(1992)005<0354:LASHFA>2.0.CO;2.

Cayan, D. R. (1992c), Latent and sensible heat flux anomalies over the northern oceans: Driving the sea surface temperature, *J. Phys. Oceanogr.*, *22*(8), 859–881, doi:10.1175/1520-0485(1992)022<0859:LASHFA>2.0.CO;2.

Chang, P., L. Ji, and R. Saravanan (2001), A hybrid coupled model study of tropical Atlantic variability, *J. Clim.*, *14*(3), 361–390, doi:10.1175/1520-0442(2001)013<0361:AHCMSO>2.0.CO;2.

Cheng, X. H., and T. J. Dunkerton (1995), Orthogonal rotation of spatial patterns derived from singular-value decomposition analysis, *J. Clim.*, *8*(11), 2631–2643, doi:10.1175/1520-0442(1995)008<2631:OROSPD>2.0.CO;2.

Deser, C., and M. S. Timlin (1997), Atmosphere-ocean interaction on weekly timescales in the North Atlantic and Pacific, *J. Clim.*, *10*(3), 393–408, doi:10.1175/1520-0442(1997)010<0393:AOIOWT>2.0.CO;2.

Deser, C., M. A. Alexander, S.-P. Xie, and A. S. Phillips (2010), Sea surface temperature variability: Patterns and mechanisms, *Annu. Rev. Mar. Sci.*, *2*, 115–143, doi:10.1146/annurev-marine-120408-151453.

Frankignoul, C. (1985), Sea surface temperature anomalies, planetary-waves, and air-sea feedback in the middle latitudes, *Rev. Geophys.*, *23*(4), 357–390, doi:10.1029/RG023i004p00357.

Frankignoul, C., and K. Hasselmann (1977), Stochastic climate models, II, Application to sea-surface temperature anomalies and thermocline variability, *Tellus*, *29*(4), 289–305, doi:10.1111/j.2153-3490.1977.tb00740.x.

Frankignoul, C., and E. Kestenare (2002), The surface heat flux feedback. Part I: Estimates from observations in the Atlantic and the North Pacific, *Clim. Dyn.*, *19*(8), 633–647, doi:10.1007/s00382-002-0252-x.

Frankignoul, C., A. Czaja, and B. L'Heveder (1998), Air-sea feedback in the North Atlantic and surface boundary conditions for ocean models, *J. Clim.*, *11*(9), 2310–2324, doi:10.1175/1520-0442(1998)011<2310:ASFITN>2.0.CO;2.

Frankignoul, C., E. Kestenare, M. Botzet, A. F. Carril, H. Drange, A. Pardaens, L. Terray, and R. Sutton (2004), An intercomparison between the surface heat flux feedback in five coupled models, COADS and the NCEP reanalysis, *Clim. Dyn.*, *22*(4), 373–388, doi:10.1007/s00382-003-0388-3.

García-Soto, C., R. D. Pingree, and L. Valdés (2002), Navidad development in the southern Bay of Biscay: Climate change and swoddy structure from remote sensing and in situ measurements, *J. Geophys. Res.*, *107*(C8), 3118, doi:10.1029/2001JC001012.

Hanley, D., M. Bourassa, J. O'Brien, S. Smith, and E. Spade (2003), A quantitative evaluation of ENSO indices, *J. Clim.*, *16*(8), 1249–1258, doi:10.1175/1520-0442(2003)16<1249:AQEOEI>2.0.CO;2.

Hasselmann, K. (1976), Stochastic climate models, I. Theory, *Tellus*, *28*(6), 473–485.

Kalnay, E., et al. (1996), The NCEP/NCAR 40-year reanalysis project, *Bull. Am. Meteorol. Soc.*, *77*(3), 437–471, doi:10.1175/1520-0477(1996)077<0437:TNYRP>2.0.CO;2.

Koutsikopoulos, C., and B. Le Cann (1996), Physical processes and hydrological structures related to Bay of Biscay anchovy, *Sci. Mar.*, *60*, 9–19.

Large, W. G., and S. G. Yeager (2004), Diurnal to decadal global forcing for ocean and sea-ice models: The data sets and flux climatologies, *NCAR Tech. Note, NCAR/TN-460+STR*, Natl. Cent. for Atmos. Res., Boulder, Colo.

Lazure, P., and A. M. Jegou (1998), 3D modelling of seasonal evolution of Loire and Gironde plumes on Biscay Bay continental shelf, *Oceanol. Acta*, *21*(2), 165–177, doi:10.1016/S0399-1784(98)80006-6.

Lazure, P., F. Dumas, and C. Vrignaud (2008), Circulation on the Armorican shelf (Bay of Biscay) in autumn, *J. Mar. Syst.*, *72*(1–4), 218–237, doi:10.1016/j.jmarsys.2007.09.011.

Le Boyer, A., G. Cambon, N. Daniault, S. Herbette, B. Le Cann, L. Marie, and P. Morin (2009), Observations of the Ushant tidal front in September 2007, *Cont. Shelf Res.*, *29*(8), 1026–1037, doi:10.1016/j.csr.2008.12.020.

Mariette, V., and B. Le Cann (1985), Simulation of the formation of Ushant thermal front, *Cont. Shelf Res.*, *29*(8), 1026–1037, doi:10.1016/0278-4343(85)90034-2.

Marshall, J. C., A. J. G. Nurser, and R. G. Williams (1993), Inferring the Subduction Rate and Period over the North-Atlantic, *J. Phys. Oceanogr.*, *23*(7), 1315–1329, doi:10.1175/1520-0485(1993)023<1315:ITSRAP> 2.0.CO;2.

Mo, R. P. (2003), Efficient algorithms for maximum covariance analysis of datasets with many variables and fewer realizations: A revisit, *J. Atmos. Oceanic Technol.*, *20*(12), 1804–1809, doi:10.1175/1520-0426(2003)020<1804:EAFMCA>2.0.CO;2.

New, A. L. (1988), Internal tidal mixing in the Bay of Biscay, *Deep Sea Res., Part A*, *35*(5), 691–709, doi:10.1016/0198-0149(88)90026-X.

North, G. R., T. L. Bell, R. F. Cahalan, and F. J. Moeng (1982), Sampling errors in the estimation of empirical orthogonal functions, *Monthly Weather Rev.*, *110*(7), 699–706, doi:10.1175/1520-0493(1982)110<0699:SEITEO> 2.0.CO;2.

Park, S., C. Deser, and M. A. Alexander (2005), Estimation of the surface heat flux response to sea surface temperature anomalies over the global oceans, *J. Clim.*, *18*(21), 4582–4599, doi:10.1175/JCLI3521.1.

Pingree, R. D., and A. L. New (1995), Structure, seasonal development and sunglint spatial coherence of the internal tide on the Celtic and Armorican shelves and in the Bay of Biscay, *Deep Sea Res., Part I*, *42*(2), 245–284, doi:10.1016/0967-0637(94)00041-P.

Pingree, R. D., G. T. Mardell, and A. L. New (1986), Propagation of internal tides from the upper slopes of the Bay of Biscay, *Nature*, *321*(6066), 154–158, doi:10.1038/321154a0.

Puillat, I., P. Lazure, A. M. Jegou, L. Lampert, and P. I. Miller (2004), Hydrographical variability on the French continental shelf in the Bay of Biscay, during the 1990s, *Cont. Shelf Res.*, *24*(10), 1143–1163, doi:10.1016/j.csr.2004.02.008.

Puillat, I., P. Lazure, A. M. Jegou, L. Lampert, and P. Miller (2006), Mesoscale hydrological variability induced by northwesterly wind on the French continental shelf of the Bay of Biscay, *Sci. Mar.*, *70*(1), 15–26, doi:10.3989/scimar.2006.70s115.

Shaman, J., and E. Tziperman (2011), An atmospheric teleconnection linking ENSO and southwestern European precipitation, *J. Clim.*, *24*(1), 124–139, doi:10.1175/2010JCLI3590.1.

Simmons, A., S. Uppala, S. Dee, and S. Kobayashi (2007), ERA-Interim: New ECMWF reanalysis products from 1989 onwards, *ECMWF Newsl.*, *110*, 25–35.

Simpson, J. H., and J. R. Hunter (1974), Fronts in Irish Sea, *Nature*, *250*(5465), 404–406, doi:10.1038/250404a0.

Uppala, S. M., et al. (2005), The ERA-40 re-analysis, *Q. J. R. Meteorol. Soc.*, *131*(612), part b, 2961–3012, doi:10.1256/qj.04.176.

von Storch, H., and F. W. Zwiers (1999), *Statistical Analysis in Climate Research*, Cambridge Univ. Press, Cambridge, U. K., doi:10.2277/0511037538.

von Storch, J. S. (2000), Signatures of air-sea interactions in a coupled atmosphere-ocean GCM, *J. Clim.*, *13*(19), 3361–3379, doi:10.1175/1520-0442(2000)013<3361:SOASII>2.0.CO;2.

Wilks, D. S. (2006), *Statistical Methods in the Atmospheric Sciences*, *Int. Geophys. Ser.*, vol. 59, Academic Press, New York, doi:10.1002/met.16.

Worley, S. J., S. D. Woodruff, R. W. Reynolds, S. J. Lubker, and N. Lott (2005), ICOADS release 2.1 data and products, *Int. J. Climatol.*, *25*(7), 823–842, doi:10.1002/joc.1166.

Yu, L., and R. A. Weller (2007), Objectively analyzed air-sea heat fluxes for the global ice-free oceans (1981–2005), *Bull. Am. Meteorol. Soc.*, *88*(4), 527–539, doi:10.1175/BAMS-88-4-527.

Zhang, Y. C., W. B. Rossow, A. A. Lacis, V. Oinas, and M. I. Mishchenko (2004), Calculation of radiative fluxes from the surface to top of atmosphere based on ISCCP and other global data sets: Refinements of the radiative transfer model and the input data, *J. Geophys. Res.*, *109*, D19105, doi:10.1029/2003JD004457.